The Astrophysical Journal, 753:23 (10pp), 2012 July 1 doi:10.1088/0004-637X/753/1/23

HerMES: A STATISTICAL MEASUREMENT OF THE REDSHIFT DISTRIBUTION OF HERSCHEL-SPIRE SOURCES USING THE CROSS-CORRELATION TECHNIQUE

K. Mitchell-Wynne[1], A. Cooray[1,2], Y. Gong[1], M. Béthermin[3,4], J. Bock[2,5], A. Franceschini[6], J. Glenn[7,8], M. Griffin[9], M. Halpern[10], L. Marchetti[6], S. J. Oliver[11], M. J. Page[12], I. P'erez-Fournon[13,14], B. Schulz[2], D. Scott[10], J. Smidt[1], A. Smith[11], M. Vaccari[6,15], L. Vigroux[16], L. Wang[11], J. L. Wardlow[1], and M. Zemcov[2,5]

[1] Department of Physics & Astronomy, University of California, Irvine, CA 92697, USA
[2] Division of Physics, Mathematics, and Astronomy, California Institute of Technology, 1200 E. California Blvd., Pasadena, CA 91125, USA
[3] Institut d'Astrophysique Spatiale (IAS), bat121, F-91405 Orsay, France
[4] Laboratoire AIM-Paris-Saclay, CEA/DSM/Irfu-CNRS-Universite Paris Diderot, CE-Saclay, pt courrier 131, F-91191 Gif-sur-Yvette, France
[5] Jet Propulsion Laboratory, 4800 Oak Grove Drive, Pasadena, CA 91109, USA
[6] Dipartimento di Astronomia, Università di Padova, vicolo Osservatorio, 3, 35122 Padova, Italy
[7] Center for Astrophysics and Space Astronomy 389-UCB, University of Colorado, Boulder, CO 80309, USA
[8] Department of Astrophysical and Planetary Sciences, CASA 389-UCB, University of Colorado, Boulder, CO 80309, USA
[9] School of Physics and Astronomy, Cardiff University, Queens Buildings, The Parade, Cardiff CF24 3AA, UK
[10] Department of Physics & Astronomy, University of British Columbia, 6224 Agricultural Road, Vancouver BC V6T 1Z1, Canada
[11] Astronomy Centre, Department of Physics & Astronomy, University of Sussex, Brighton BN1 9QH, UK
[12] Mullard Space Science Laboratory, University College London, Holmbury St. Mary, Dorking, Surrey RH5 6NT, UK
[13] Instituto de Astrofísica de Canarias (IAC), E-38200 La Laguna, Tenerife, Spain
[14] Departamento de Astrofísica, Universidad de La Laguna (ULL), E-38205 La Laguna, Tenerife, Spain
[15] Astrophysics Group, Physics Department, University of the Western Cape, Private Bag X17, 7535 Bellville, Cape Town, South Africa
[16] Institut d'Astrophysique de Paris, UMR 7095, CNRS, UPMC University of Paris 06, 98bis Boulevard Arago, F-75014 Paris, France
Received 2012 February 29; accepted 2012 April 24; published 2012 June 11

ABSTRACT

The wide-area imaging surveys with the *Herschel Space Observatory* at submillimeter (sub-mm) wavelengths have now resulted in catalogs of the order of one-hundred-thousand dusty, starburst galaxies. These galaxies capture an important phase of galaxy formation and evolution, but, unfortunately, the redshift distribution of these galaxies, $N(z)$, is still mostly uncertain due to limitations associated with counterpart identification at optical wavelengths and spectroscopic follow-up. We make a statistical estimate of $N(z)$ using a clustering analysis of sub-mm galaxies detected at each of 250, 350 and 500 μm from the *Herschel* Multi-tiered Extragalactic Survey centered on the Boötes field. We cross-correlate *Herschel* galaxies against galaxy samples at optical and near-IR wavelengths from the Sloan Digital Sky Survey, the NOAO Deep Wide Field Survey, and the *Spitzer* Deep Wide Field Survey. We create optical and near-IR galaxy samples based on their photometric or spectroscopic redshift distributions and test the accuracy of those redshift distributions with similar galaxy samples defined with catalogs from the Cosmological Evolution Survey (COSMOS), which has superior spectroscopic coverage. We model the clustering auto- and cross-correlations of *Herschel* and optical/IR galaxy samples to estimate $N(z)$ and clustering bias factors. The $S_{350} > 20$ mJy galaxies have a bias factor varying with redshift as $b(z) = 1.0^{+1.0}_{-0.5}(1+z)^{1.2^{+0.3}_{-0.7}}$. This bias and the redshift dependence is broadly in agreement with galaxies that occupy dark matter halos of mass in the range of 10^{12} to 10^{13} $M_{\odot}$. We find that galaxy selections in all three Spectral and Photometric Imaging Receiver (SPIRE) bands share a similar average redshift, with $\langle z \rangle = 1.8 \pm 0.2$ for 250 μm selected samples, and $\langle z \rangle = 1.9 \pm 0.2$ for both 350 and 500 μm samples, while their distributions behave differently. For 250 μm selected galaxies we find the a larger number of sources with $z \leqslant 1$ when compared with the subsequent two SPIRE bands, with 350 and 500 μm selected SPIRE samples having peaks in $N(z)$ at progressively higher redshifts. We compare our clustering-based $N(z)$ results to sub-mm galaxy model predictions in the literature, and with an estimate of $N(z)$ using a stacking analysis of COSMOS 24 μm detections.

Key words: galaxies: evolution – galaxies: high-redshift – submillimeter: galaxies

Online-only material: color figures

1. INTRODUCTION

The properties of the dusty, star-forming galaxies detected by the Spectral and Photometric Imaging Receiver (SPIRE; Griffin et al. 2010) aboard the *Herschel Space Observatory*[17] (Pilbratt et al. 2010) at submillimeter (sub-mm) wavelengths provide important clues to the nature of dusty star formation and the role of galaxy mergers in triggering such star formation in distant galaxies. However, the redshift distribution of these galaxies has yet to be determined observationally. The low spatial resolution of *Herschel*-SPIRE observations complicates the identification of counterparts at optical and near-IR wavelengths. Moreover, the optical emission from these star-bursting galaxies is highly extinct and could potentially bias optical spectroscopy observations to low-redshift bright galaxies. Instead of optical or IR spectroscopy, millimeter (mm) and sub-mm wave spectroscopy can be pursued targeting fine-structure and molecular lines such

[17] *Herschel* is an ESA space observatory with science instruments provided by European-led Principal Investigator consortia and with important participation from NASA.

as CO and [C II]. Such measurements, unfortunately, are currently limited to a handful of the brightest sources—mostly the rarely lensed sub-mm galaxies (e.g., Lupu et al. 2010; Scott et al. 2011; Riechers et al. 2011; Harris et al. 2012), as existing instrumental capabilities do not allow large CO or [C II] surveys of typical sub-mm galaxies.

There have been a few other approaches to obtain the $N(z)$ of sources at these wavelengths. A statistical approach based on photometry alone, using SPIRE colors, was considered in Amblard et al. (2010; see also Lapi et al. 2011), but such techniques are subject to uncertainties on the assumed spectral energy distribution (SED) of the galaxies at sub-mm wavelengths. These generally involve isothermal SED models, where the redshift distribution is degenerate with the assumed dust temperature distribution. Marsden et al. (2009) employed stacking methods to effectively measure the CIB as a function of redshift, and Béthermin et al. (2012) have recently measured deep source counts as a function of redshift, also via stacking, which is compared to with results of this paper.

Here, we pursue a second statistical approach to measure the SPIRE galaxy redshift distribution using the spatial clustering of the sub-mm population relative to clustering of galaxies with an a priori known redshift distribution (Schneider et al. 2006; Newman 2008; Zhang et al. 2010). The unknown sub-mm redshift distribution can be estimated via the strength of its cross-correlation relative to galaxy samples of known redshifts. Modeling also requires that the clustering bias factors of all galaxies be determined jointly through a combination of auto- and cross-correlation functions. The key advantage of this technique is that it does not require cross-identification of SPIRE sources in optical and IR catalogs.

For this study we make use of data from the *Herschel* Multi-tiered Extragalactic Survey (HerMES; Oliver et al. 2012), which mapped a large number of well-known fields with existing multi-wavelength ancillary data using SPIRE. To cross-correlate against SPIRE-selected galaxies, we make use of near-IR-selected galaxy samples from *Spitzer* observations based on the 1.6 μm "bump," which has long been established as a redshift indicator (Sawicki 2002; Simpson & Eisenhardt 1999; Wright et al. 1994). The bump results from the fact that the H^- absorption in stellar atmospheres is minimally opaque at 1.6 μm. This leads to a bump in the SEDs of cool stars at 1.6 μm (John 1988) that is nearly ubiquitous in galaxy spectra. For $z > 0$, the wavelength at which the bump in the SED peaks allows for a redshift determination based on the colors in IRAC channels between 3.6 and 8 μm, and covering the redshift range of 1–2.5. We complement these "bump" galaxy samples with a 24 μm and an R-band based sample of dust obscured galaxies (DOGs), which has a redshift distribution that peaks around $z \sim 2.3$ (Dey et al. 2008). We also make use of optical-selected galaxy samples with Sloan Digital Sky Survey (SDSS) spectroscopic and photometric redshifts out to about 0.7.

The paper is organized as follows. In Section 2, we describe source selection in SPIRE and galaxy sample selection with IRAC and MIPS bands, complemented with optical data to remove outliers. In Section 3, we describe the redshift distribution of the galaxy samples used for the cross-correlation analysis, and in Section 4 we describe the cross-clustering measurements. Fitting results are presented in Section 5. In Section 6, we present $N(z)$ and $b(z)$ and discuss our results. We assume a flat-ΛCDM cosmological model and fix the cosmological parameters to the best-fit values of $\Omega_m = 0.27$, $\Omega_b = 0.046$, $\sigma_8 = 0.81$, $n_s = 0.96$, and $h = 0.71$ (Komatsu et al. 2011) when performing Markov Chain Monte Carlo (MCMC) model fits.

2. SPIRE SOURCE AND GALAXY SAMPLE SELECTION

2.1. Herschel-SPIRE sample

The HerMES SPIRE source catalogs used for this paper come from a combined analysis involving both a direct source extraction and an attempt to account for blending at 350 and 500 μm wavelengths given the positions of 250 μm detections (L. Wang et al. 2012, in preparation). The method updates the source extraction pursued by HerMES at each of the three SPIRE bands independently that ignored issues associated with blending at longer wavelengths (Smith et al. 2012).

In order to maximize the overlap with multi-wavelength data, we concentrate our study on the Boötes field with HerMES SPIRE data covering 12.5 deg^2. The field has been imaged with *Spitzer* IRAC as part of the *Spitzer* Deep Wide Field Survey (SDWFS; Ashby et al. 2009) and from the ground with optical to near-IR observations as part of the NOAO Deep Wide Field Survey (NDWFS; Jannuzi & Dey 1999), with coverage also provided by the SDSS (Abazajian et al. 2009).

For this study, we selected SPIRE sources with a flux density greater than 20 mJy in the Böotes field. We find in excess of 22,000 sources in each of the SPIRE bands covering the entire 12.5 deg^2 of SPIRE observations, while 3775, 3243, and 958 galaxies at 250 μm, 350 μm, and 500 μm, respectively, were used in the cross-correlation study—an area covering 6.7 deg^2, where various ancillary data best overlap.

At 20 mJy, the SPIRE catalogs are ∼30% complete at each of the three wavelengths. The 90% completeness of the catalogs is at a flux density of about 55 mJy (L. Wang et al. 2012, in preparation). At such a high flux density level, the number of SPIRE sources in the area overlapping with ancillary data is down by at least factor of eight and the resulting low surface density does not allow useful constraints on the redshift distribution. We note some caution in interpreting our results with models due to the incompleteness. We are unable to correct for it through simulations due to the lack of a priori information on the redshift distribution of missing sources. It is unlikely, however, that the redshift distributions presented here are biased due to catalog incompleteness since the source detection algorithm is primarily based on the flux density and not the individual redshifts of SPIRE sources.

2.2. IRAC Sample Selection and Star–Galaxy Separation

Using the SDWFS data combined with ground-based K-band data from NDWFS, we generated three different catalogs of 1.6 μm bump sources based on the IRAC channel where the SED peaks. These three samples are as follows: bump-1 with a peak in the 3.6 μm channel ($0.5 \lesssim z \lesssim 1.5$), bump-2 peaking in the 4.5 μm channel ($0.8 \lesssim z \lesssim 2.2$), and bump-3 with a peak at 5.8 μm ($1.5 \lesssim z \lesssim 3.0$). Using the photometric redshifts computed via a template fitting method (Csabai et al. 2003) in the SDSS DR7 catalog, we also constructed two separate redshift distributions with peaks at $z \sim 0.3$ and 0.7.

In order to establish catalogs of bump-1 to bump-3 galaxy populations we first had to remove stars and other contaminants from our optical and IR catalogs. This was done using a combination of infrared and optical data. We used the SDWFS four-epoch stacked catalog (Ashby et al. 2009) which contains all sources detected in the first channel of IRAC at or above 5σ.

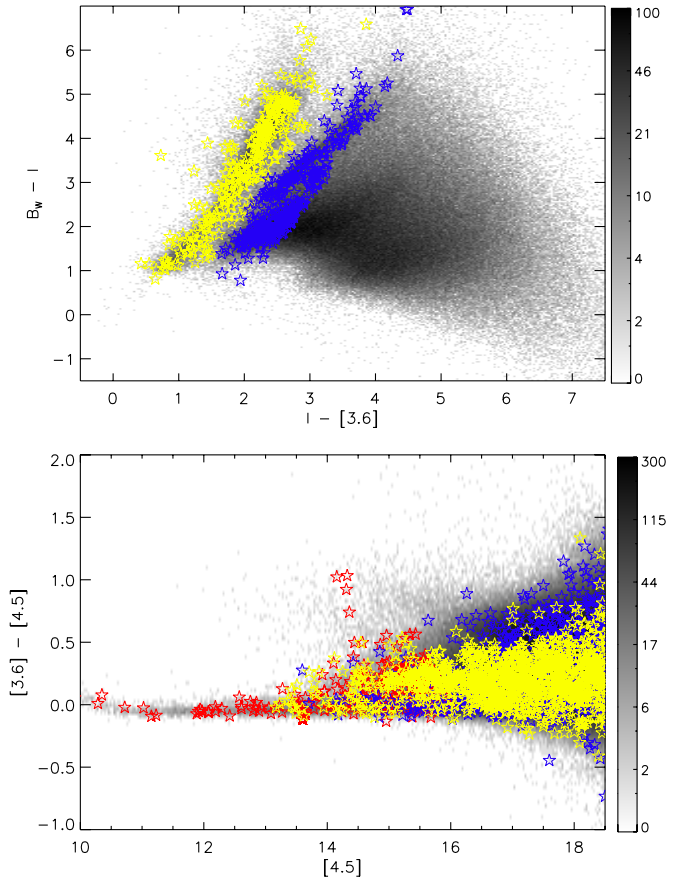

Figure 1. Color–color (top: $B_w - I$ vs. $I - [3.6]$) and color–magnitude (bottom: $[3.6] - [4.5]$ vs. [4.5]) density plots of sources (both stars and galaxies) in our Boötes field catalogs. Red stars indicate the 3.6 μm magnitude selection for stars, while giants are depicted as yellow stars, and the *BIK* sequence as blue stars (see Section 2.2 for details). Only a fraction of the sources identified as stars are plotted to avoid overcrowding in the plots. Black points are the galaxies.

(A color version of this figure is available in the online journal.)

This catalog was matched with the NDWFS third data release catalog and the SDSS catalog, using a 2.″5 matching radius. For sources with multiple matches (<3%), magnitudes from the NDWFS catalog were then compared with the 3.6 μm magnitude and entries with the most similar values were kept.

Stars and spurious sources were removed from the resulting merged catalog using various techniques. Vega magnitudes and 6″ diameter aperture photometry are used throughout the star–galaxy separation unless otherwise noted. We employed a three stage process to remove stars from our catalog. An initial selection of sources with $[3.6] < 16$ were identified as stars, where [3.6] represents the vega magnitude at 3.6 μm. Using the combination of optical and IRAC photometry we further classify sources as stars that either satisfy $(B_w - I) > 2(I - [3.6]) - 1.65$ or $-1.65 > (B_w - I) - 2(I - [3.6]) > -3.35$ (Eisenhardt et al. 2004). The former criterion defines a sequence of *BIK* stars (Huang et al. 1997) and the latter a sequence of giant stars (Johnson 1966; Bessell & Brett 1988). Lastly, for IRAC sources without optical counterparts, we used a binning method that involved only the IRAC bands (Waddington et al. 2007). Three flux density bins were defined with the criteria $[3.6] \leqslant 19.5$, $19.5 < [4.5] \leqslant 20.0$, and $[4.5] \leqslant 23$, with color cuts [3.6]–[4.5] < -0.35, -0.30, and -0.25, respectively, all sources satisfying these criteria were assumed to be stars. The results of these extractions are shown in Figure 1.

2.3. Bump, DOG, and SDSS Selections

From our resulting merged and star-subtracted catalog, we invoked simple color constraints to classify three different types of bump sources and DOGs (Dey et al. 2008), using 4″ aperture diameter photometry. Bump-1, bump-2, and bump-3 sources each display excess emission in IRAC channels 1, 2, and 3, respectively. Bump-1 sources were selected using the criteria $K - [3.6] > 0.1$ and $[3.6] - [4.5] < 0$; bump-2 with $K - [3.6] > 0$, $[3.6] - [4.5] > 0$, and $[4.5] - [5.8] < 0$; bump-3 with $[3.6] - [4.5] > 0$, $[4.5] - [5.8] > 0$, and $[5.8] - [8] < 0$. The number of bump-1 sources in the SDWFS catalogs were found to be $\sim 1.3 \times 10^4$ at the 5σ detection limit of the 3.6 μm channel of the IRAC instrument. Bump-2 source identification yielded 6.5×10^3 galaxies, while the bump-3 catalog contains 4×10^3 galaxies.

We also make use of a sample of DOGs, selected with 24 μm *Spitzer*-MIPS and optical *R*-band data to have extreme red colors from dust obstruction, with $S_{24}/S_R > 1000$ (where S_{24} is the 24 μm flux density) or equivalently $R - [24] \geqslant 14$ and $S_{24} \geqslant 0.3$ mJy ($\approx 6\sigma$; Dey 2009). We found that a total of 2838 galaxies satisfied the selection criteria. Based on spectroscopic follow-up, they are now known to have a mean redshift around $z \sim 2.3$ (Dey 2009). We make use of the full, broad redshift distribution for this sample, spanning the range of $0.5 < z < 3.5$, with a peak around $z \sim 2$, found from a similar identification of DOGs in the Cosmological Evolution Survey (COSMOS) field (see Section 3 and Figure 2) for the present analysis. These DOGs have been suggested to be an intermediary phase of the evolution of quasi-stellar objects from gas-rich mergers (Dey 2009). They have also been shown to be strongly clustered and are believed to be progenitors of massive $(3 - 6L_*)$ galaxies at low redshift (Browdin et al. 2008).

Finally, to cover the redshift range of $0 < z < 0.7$ efficiently we also selected optical galaxies from SDSS. These sources have photometric redshifts, individually determined with SED fits to SDSS photometry, in the above range. We make use of 8000 SDSS galaxies and we consider two sub-samples peaking at $z \sim 0.2$ and 0.5 with roughly equal numbers. The first of these two sub-samples is obtained by selecting sources which obey $2.6 < B - I < 3$ and $-0.8 < I - R < 0.1$, while the second selection obeys $B - I > 4$ and $-0.9 < I - R < 0$. These six galaxy samples (three bump catalogs, DOGs, and two SDSS samples) provide adequate redshift coverage over the range of $0 < z < 3$.

3. COSMOS PHOTO-z AND SPEC-z

While we are able to generate large samples of galaxies to cross-correlate against the SPIRE catalogs of the Boötes field, the existing spectroscopic and photometric redshift information in the Boötes field is not adequate to establish the redshift distributions of the *Spitzer* galaxy samples. For that we turn to data in the COSMOS (Scoville et al. 2006; Capak et al. 2007) where we can select similar galaxy samples as in the Boötes field, using the same depth and color criteria. For those galaxies we are able to use either the existing spectroscopic or the photometric redshifts from the public COSMOS catalog (Ilbert et al. 2009). We assume that the redshift distributions for galaxy samples in COSMOS are the same as for Boötes when interpreting clustering measurements from the wider Boötes area that overlaps with SPIRE.

The COSMOS field has extensive photometric redshift measurements over 2 deg^2 using 30 broad, intermediate, and

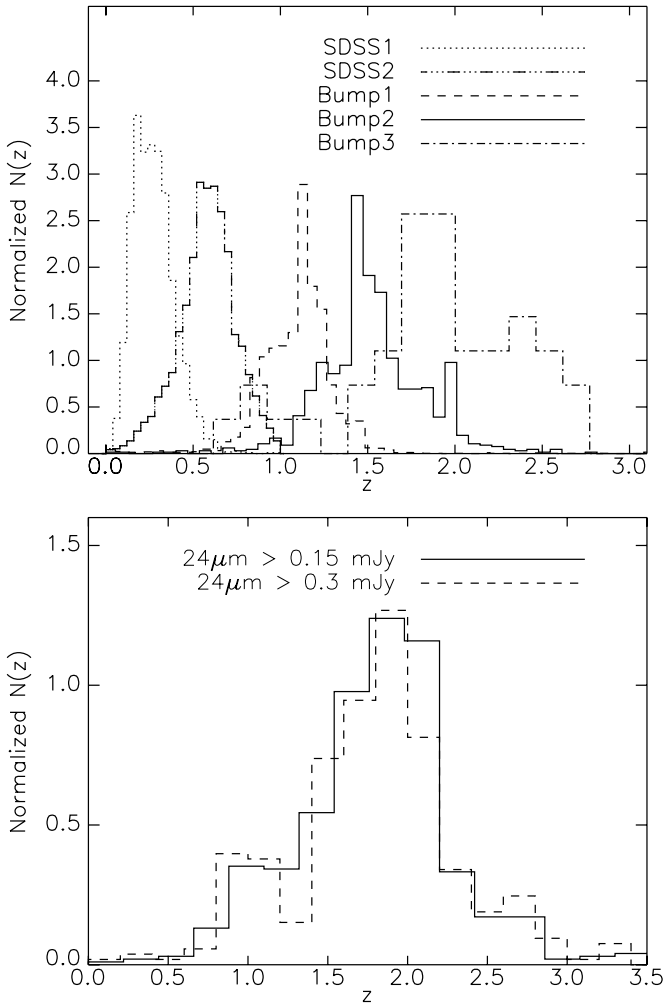

Figure 2. $N(z)$ distribution obtained from SDSS photometric redshifts in the Boötes field as well as bump-1 to bump-3 (top plot) and DOGs' (bottom plot) redshift distributions from the COSMOS field. We assume the latter four redshift distributions measured directly in COSMOS are also applicable for galaxy samples under the same color selection criteria in the Boötes field.

narrow band filters from space-based telescopes (*Hubble, Spitzer, GALEX, XMM, Chandra*) and ground-based telescopes (Subaru, VLA, ESO-VLT, UKIRT, NOAO, CFHT, and others). We used a public COSMOS source catalog containing $\sim 10^4$ spectroscopic redshifts, and $\sim 3 \times 10^5$ photometric redshifts that were computed using a χ^2 galaxy template-fitting technique (Ilbert et al. 2009). In both the Böotes and COSMOS fields, we imposed the same brightness thresholds in the selection bands: for IRAC channel 1 and K band we imposed a 5σ detection limit. We require that each of the galaxies detected at above 5σ is also detected in IRAC Channels 2–4. In those cases, however, we considered a source that has a flux density above 50% completeness level to be considered as detected, while sources with flux densities below 50% completeness level of each of the three channels were dropped from the final catalog. This selection process was chosen to ensure that we are probing equal depths between the two fields, COSMOS and Böotes.

Using the same selection methods described above, we were able to obtain $N(z)$ measurements for each of our different source classifications from the COSMOS source catalog (see Figure 2). Note that the galaxy type selections are mutually exclusive, so there are no overlapping sources between different samples. All of the bump sources have well-defined redshift distributions, and the DOG distribution agrees well with those in the literature (see Figure 1 in Dey 2009). We identified 384 sources as DOGs in COSMOS, with $S_{24} > 0.3\ \mu$Jy and 683 with $S_{24} > 0.15\ \mu$Jy, a number density consistent with statistics of the DOG population in other fields (Browdin et al. 2008).

4. ANGULAR CROSS-CORRELATION AND COVARIANCE MATRIX

To obtain the redshift distributions of SPIRE sources, we first cross-correlate the SDSS-selected sample and bumps and DOGs from the Boötes field, against sub-mm sources in each SPIRE band, from arcminute to degree angular scales. We also measure the autocorrelation functions of the galaxy and SPIRE samples, as these are needed to model the clustering strength and to extract the unknown redshift distribution.

We use a bootstrap method to establish the covariance matrix for each of the cross- or auto-correlation functions, as an accounting of the covariance is needed to properly model the clustering measurements. We do this by selecting 200 separate catalogs from the original SPIRE data by removing about 5% of the sources randomly. We measure the auto and cross-correlations with each of those catalogs and build the mean auto and cross-correlation functions, the variance from the scatter, and the covariance from the correlations between the measured auto and cross-correlation functions.

The angular cross-correlation function is modeled analytically using the COSMOS redshift distribution of the bump-1, bump-2, bump-3, and DOGs, while for the SDSS galaxy samples we make use of the public photometric redshifts from SDSS DR-7. For simplicity we bin the unknown SPIRE redshift distribution from $z = 0$ to 4 in five bins in redshift. To extract the best-fit values and uncertainties in the redshift distribution bins, and the other parameters in the analytical model, we make use of a likelihood fitting technique based on the MCMC method.

In this section, we first discuss the method of modeling the angular cross-correlation $w_{\rm cross}$ using the redshift distribution of galaxies and the linear matter power spectrum. Then we describe the measurement of the $w_{\rm cross}$ functions as well as the covariance matrix from the galaxy samples.

4.1. Modeling the Angular Cross-correlation

The angular cross-correlation function $w_{\rm cross}$ for two galaxy samples is defined by

$$w_{\rm cross}(\theta) = \langle \delta n_1(\hat{\phi}) \delta n_2(\hat{\phi}') \rangle, \quad (1)$$

where $\delta n_i(\hat{\phi}) = (n_i(\hat{\phi}) - \bar{n}_i)/\bar{n}_i$, with $n_i(\hat{\phi})$ being the number density of galaxies observed in direction $\hat{\phi}$ in the sky ($\theta = \phi - \phi'$) and $\bar{n}_i$ being the mean number density of the galaxy sample i. δn_i can be decomposed into two terms—one term from the real clustering of galaxies and a second term caused by lensing magnification. Here, we ignore the few percent contribution from lensing (Wang et al. 2011) and only consider the clustering term, which is

$$w_{\rm gg}(\theta) = b_1\, b_2 \int_0^{\chi_{\rm H}} d\chi\, N_1(\chi) N_2(\chi) \times \int_0^{\infty} \frac{k}{2\pi} P(\chi, k) J_0[kr(\chi)\theta], \quad (2)$$

where b_1 and b_2, $N_1(\chi)$ and $N_2(\chi)$ are the galaxy bias and the normalized radial distribution for the two galaxy samples,

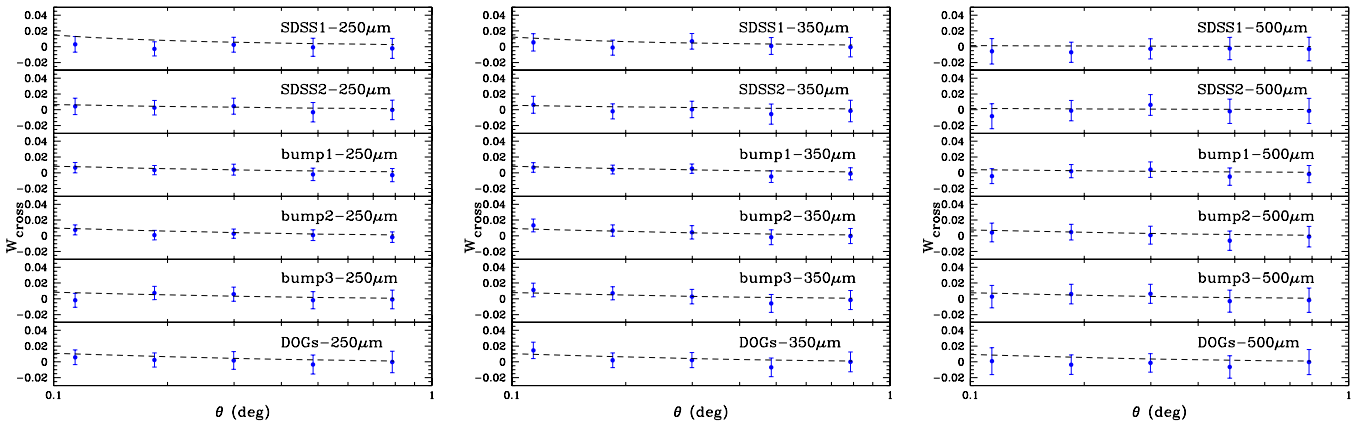

Figure 3. Angular cross-correlation between the 250, 350, and 500 μm objects of the SPIRE surveys and the SDSS1, SDSS2, bump-1, bump-2, bump-3, and DOGs in the Boötes field. The 1σ error bars are derived from 200 bootstrap realizations. The black dashed lines are theoretical estimates of the angular cross-correlation using the best-fit value of the SPIRE redshift distribution.

(A color version of this figure is available in the online journal.)

respectively. $P(\chi, k)$ is the power spectrum of the dark matter, $J_0(x) = \sin(x)/x$ is the zero-order Bessel function, and χ and $r(\chi)$ are the radial comoving distance and the comoving angular diameter distance, respectively, ($r(\chi) = \chi$ in flat space). χ_H denotes the radial distance to the horizon or Hubble length. Note that $w_{gg}(\theta)$ will be zero if the positions of the two galaxy samples do not overlap with each other.

When modeling the measurements, we make use of the linear theory power spectrum to describe $P(\chi, k)$ and focus only on modeling the measurements over the angular scales of 6′, and above where the clustering is in the linear regime (Cooray et al. 2000). At these large angular scales, the 1-halo term makes less than a 1% correction to the correlation function and can be safely ignored.

4.2. The Measurement and Covariance Matrix of the Angular Cross-correlation

The angular cross-correlation function $w_{\rm cross}(\theta)$ is defined as the fractional excess of the probability relative to a random distribution (Peebles 1980), and can be measured from galaxy samples by the *pair counts* method. There are several kinds of estimators that are proposed to measure the cross-correlation (e.g., Blake et al. 2006); the one we adopt here is the modified Landy–Szalay estimator which is derived from the auto-correlation (Landy & Szalay 1993):

$$w_{\rm cross}(\theta) = \frac{D_1D_2 - D_1R_2 - D_2R_1 + R_1R_2}{R_1R_2}, \qquad (3)$$

where $D_1D_2(\theta)$, $D_1R_2(\theta)$, $D_2R_1(\theta)$, and $R_1R_2(\theta)$ are the normalized pair counts for data (D_i) and random (R_i) catalogs with separation θ.

We generate random un-clustered catalogs with varying catalog sizes that contain 5 to 10 times more sources than the observed samples, with a larger number of sources than in data catalogs to avoid biases coming from Poisson fluctuations. The angular cross-correlation extracted from the observational data and the theoretical estimation using the best-fit value (see the next section) of the SPIRE distribution in the Boötes field are shown in Figure 3. The auto- and cross-correlations of the SPIRE surveys for 250 μm, 350 μm, and 500 μm are also shown in Figure 4.

As was mentioned in the previous section, to avoid biases coming from nonlinear clustering we only use $w(\theta)$ data from 0.1° to 1° to fit the model, since adding the 1-halo term with three or four extra parameters for the halo occupation number will result in extra degeneracies, degrading the $N(z)$ estimates, consistent with theoretical suggestions in the literature (e.g., Neyrinck et al. 2006). Also keeping to scales larger than 0.°1, we avoid the need to introduce a transfer function for $w(\theta)$ for SPIRE sources and their cross-correlations since at smallest scales close to the SPIRE point response function, clustering is expected to be affected by source blending and issues related to map making. As studied in Cooray et al. (2010), at $\theta > 0.°05$, there are no corrections to the measured $w(\theta)$.

To evaluate the covariance matrix of the angular correlation $w(\theta)$, we use a bootstrap method to generate 200 realizations for the galaxy samples. Then the covariance matrix of $w_{\rm cross}$ is

$$C_{ij} = \frac{1}{N-1}\sum_{k}^{N}[w_k(\theta_i) - \bar{w}(\theta_i)][w_k(\theta_j) - \bar{w}(\theta_j)], \qquad (4)$$

where $N = 200$ is the number of the bootstrap realization and $\bar{w}(\theta)$ is the average angular correlation for all bootstrap realizations at θ. The error of the angular correlation thus takes the form of $\sigma_w(\theta_i) = \sqrt{C_{ii}}$.

We use nine logarithmic bins from 0.°01 to 1° to calculate the angular auto- and cross-correlation and their covariance matrix. The model correlation and cross-correlation functions, $w^{\rm th}$, are calculated for a given $N(z)$ and clustering bias factors (described in the next section), and are compared with measurements, $w^{\rm data}$, using the covariance matrix from the data. In calculating $w^{\rm th}$, we make use of the measured $N(z)$ of the SDSS, bumps, and DOGs, derived in the last section.

5. ESTIMATING THE SPIRE GALAXY REDSHIFT DISTRIBUTION

We employ an MCMC technique, using the Metropolis–Hastings algorithm (Hastings 1970), to fit the SPIRE redshift distribution $N(z)$ of sources with flux densities greater than 20 mJy at each of the three wavelengths. We follow established standard procedures in fitting the data, including thinning of the chains and separation of steps that are part of the initial burn-in period.

We describe the unknown redshift distribution $N(z)$ at five values, using five "pivot" redshifts $z_{\rm p} = 0.1, 0.5, 1, 2$, and 3,

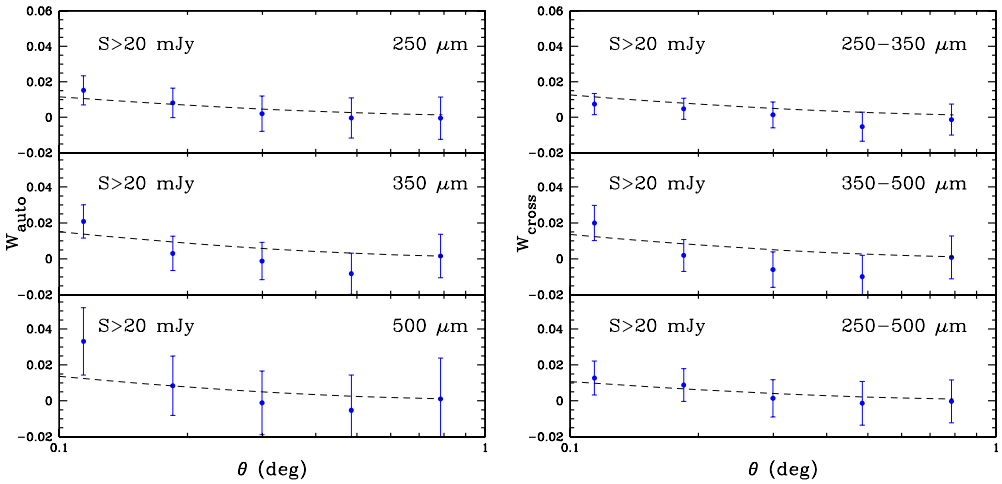

Figure 4. Angular auto- and cross-correlation for the 250, 350, and 500 μm SPIRE sources in the Boötes field. The 1σ error bars are derived from 200 bootstrap realizations. The black dashed lines are the theoretical estimation using the best-fit value of the SPIRE redshift distribution.
(A color version of this figure is available in the online journal.)

and set $N(z_p = 0) = 0$ and $N(z_p = 4) = 0$ to describe the two end points of the redshift distribution. To describe $N(z)$ when $0 < z < 4$, we linearly interpolate the fitted $N(z)$ distribution at each of the pivot redshifts z_p and use those linearly interpolated values between two pivots in our model fitting algorithm. The assumption that $N(z > 4) = 0$ does not bias our results since we only expect at most a few percent of the sub-mm galaxies to be located at $z > 4$ (e.g., Pope & Chary 2010). Furthermore, we do not have sensitivity to such high redshifts, given that the optical and near-IR galaxy samples we have used for the cross-correlation study are restricted to $z < 4$.

Before deciding on this description, we also considered a description of $N(z)$ that involved five bins in redshift, with $N(z)$ taking the same value in each of the bins. However, we failed to obtain fits to the binned case since in the first bin $0 < z < z_1$, $N(z)$ prefers a value that is non-zero at z_1, but zero at $z = 0$. The use of pivot redshifts and linear interpolation between pivots avoids the discontinuities that were present with the binned case, leading to issues with the numerical integrations of the clustering in Equation (2).

As discussed earlier (related to Equation (2)), we also need to account for the clustering bias factor of galaxies and SPIRE sources relative to the linear matter power spectrum. Instead of keeping the bias in each of the bins as a free parameter, which leads to a large number of model parameters to be determined from the data, we assume a model for the galaxy bias, as a function of redshift, to be of the form

$$b(z) = b_0(1 + z)^c, \tag{5}$$

where b_0 and c are free parameters to be determined from data using the MCMC analysis. In addition to this model we also consider two other approaches with: (1) $b(z) = b_0 + b_1 z$, a simple linear interpolation with redshift; and (2) $b(z) = b_0$ when $z < 2$ and $b(z) = b_1$ when $z > 2$. We found results consistent within 1σ uncertainties in both $N(z)$ and $b(z)$ with the power-law form when using the linear relation.

For optical and IR galaxy samples we assume that each has an average bias factor, and we do not account for the redshift evolution of the bias factor in each of the galaxy samples. This is a fair assumption since each of the samples we have created has a narrow redshift distribution compared to the distribution expected for the SPIRE galaxies.

Altogether we have 13 free parameters in our MCMC fitting, which contains 5 parameters for the SPIRE redshift distribution and 6 bias parameters for SDSS-1, SDSS-2, bump-1, bump-2, bump-3, and DOGs, plus 2 parameters to describe the SPIRE galaxy bias and its evolution with redshift. While the redshift distribution and bias factor and evolution for SPIRE sources are different at each of the three SPIRE wavelengths, the bias factors for optical and IR-selected galaxies remain the same. Thus, the six bias parameters for the galaxy samples, with assumed or known redshifts, can be determined jointly from cross-correlation data at the three SPIRE wavelengths together with their auto-correlation functions. We fix all the other cosmological parameters and assume the flat ΛCDM model as mentioned in Section 1.

We fit the data following the χ^2 distribution estimated as

$$\chi^2 = \sum_{\text{datasets}} \mathbf{\Delta}^{\mathrm{T}} \mathbf{C}^{-1} \mathbf{\Delta}, \tag{6}$$

where $\mathbf{\Delta} = [w^{\text{data}}(\theta_1) - w^{\text{th}}(\theta_1), \ldots, w^{\text{data}}(\theta_9) - w^{\text{th}}(\theta_9)]$, $\mathbf{C}$ is the covariance matrix of $w(\theta)$, w^{th} is obtained directly from the $N(z)$, and "data" here are the full angular cross-correlations for the SPIRE, SDSS-1, SDSS-2, bump-1, bump-2, bump-3, and DOG samples (21 cross-correlations for each SPIRE band), and their auto-correlations in the Boötes field. The angular auto-correlation and the cross-correlation between the SPIRE and the SDSS1, SDSS2, bump-1, bump-2, bump-3, and DOG subsamples extracted from the observational data in the Boötes field are shown in Figures 3 and 4 as examples.

We adopt an adaptive step-size Gaussian sampler given by Doran & Mueller (2004) for the MCMC fitting process. The convergence criterion we take is discussed in Gelman & Rubin (1992). We generate six chains with about 10^5 points after the convergence process. At the end we resample the chains to get about 10,000 points to illustrate the probability distribution of the parameters.

6. RESULTS AND DISCUSSION

In Figure 5, we show the best-fit results and the 1σ errors of the redshift distribution, $N(z)$, for the three SPIRE bands (see also Table 1 for the values). The redshift distributions are normalized such that $\int dz N(z) = 1$. The 1σ error bars

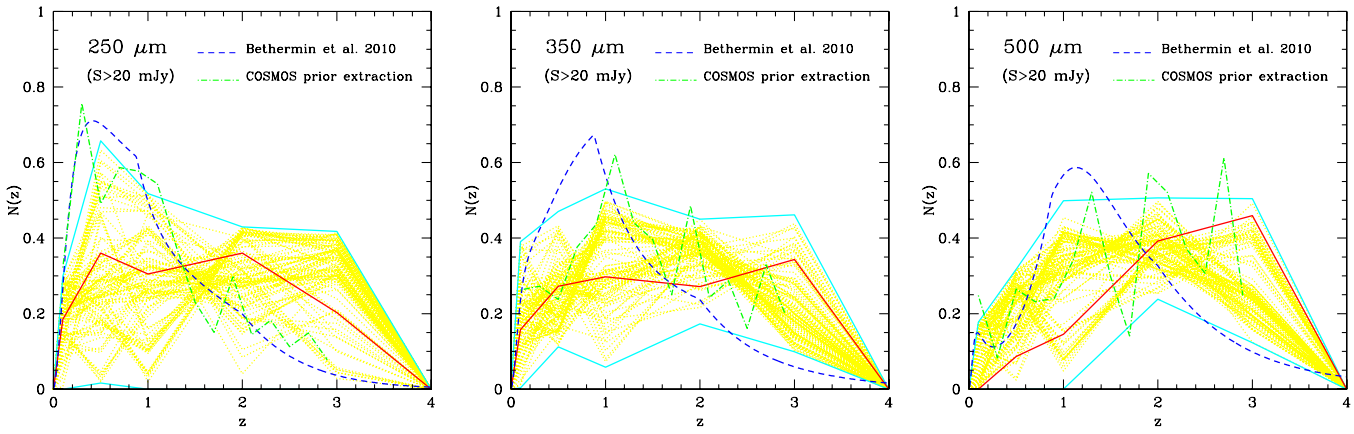

Figure 5. Best-fit normalized redshift distributions (red solid line) and 1σ error regions (cyan line) for sources with flux densities greater than 20 mJy for 250, 350 and 500 μm SPIRE bands using SDSS, bump-1 to bump-3, and DOGs catalogs in the Boötes field. As examples, 100 best-fit $N(z)$ from our MCMC results are also shown in yellow dotted lines. The analytical model predictions on $N(z)$ from the literature (blue dashed line; Béthermin et al. 2010) for galaxies in the three SPIRE bands are also shown for comparison. The green line is a direct estimate of $N(z)$ using the combination of a stacking and a cross-identification analysis involving 24 μm MIPS and SPIRE sources from Béthermin et al. (2012).

(A color version of this figure is available in the online journal.)

Table 1
The Best-fit SPIRE Redshift Distribution and Bias Parameters

$N(z)$	z-pivot	250 μm	350 μm	500 μm
N_1	0.1	$0.19^{+0.11}_{-0.19}$	$0.16^{+0.23}_{-0.15}$	$0.00^{+0.18}_{-0.00}$
N_2	0.5	$0.36^{+0.30}_{-0.34}$	$0.27^{+0.20}_{-0.16}$	$0.09^{+0.23}_{-0.09}$
N_3	1.0	$0.31^{+0.21}_{-0.31}$	$0.30^{+0.23}_{-0.24}$	$0.15^{+0.35}_{-0.15}$
N_4	2.0	$0.36^{+0.07}_{-0.36}$	$0.27^{+0.18}_{-0.10}$	$0.39^{+0.11}_{-0.15}$
N_5	3.0	$0.20^{+0.22}_{-0.20}$	$0.34^{+0.12}_{-0.24}$	$0.46^{+0.04}_{-0.34}$
Average redshift				
$\langle z \rangle$		1.8 ± 0.2	1.9 ± 0.2	1.9 ± 0.2
Sub-mm bias				
b_0		$1.0^{+0.8}_{-0.5}$	$1.0^{+1.0}_{-0.5}$	$0.9^{+0.6}_{-0.5}$
c		$1.1^{+0.4}_{-0.6}$	$1.2^{+0.3}_{-0.7}$	$1.1^{+0.5}_{-0.8}$

Table 2
Bias Factors of Optical and IR-selected Galaxy Samples

Sample	Approximate z-Range	Bias
SDSS-1	0–0.4	$1.6^{+0.2}_{-0.2}$
SDSS-2	0.3–0.7	$1.1^{+0.2}_{-0.3}$
Bump-1	0.8–1.5	$2.0^{+0.3}_{-0.3}$
Bump-2	1.2–2.0	$2.3^{+0.4}_{-0.5}$
Bump-3	1.6–2.5	$2.0^{+0.8}_{-1.1}$
DOGs	0.7–3.0	$2.6^{+1.1}_{-1.9}$

(cyan lines) are derived from the Markov Chains, which are statistically estimated via the values of $N(z)$ calculated using each chain point at different redshifts. As an example, the 100 best-fit $N(z)$ are also shown in yellow dotted lines. As shown by the errors of $N(z)$ at high redshift ($z > 3$), the galaxy distribution could be larger when going from the 250 μm to 500 μm bands, which implies there may be more high-redshift galaxies for the 500 μm band than the 250 μm and 350 μm bands. In Table 1 we also tabulate the average redshift of the SPIRE sources by calculating $\int dz\, zN(z)$, and these values range from 1.8 ± 0.2 at 250 μm to 1.9 ± 0.2 for 500 μm. We also derive the correlation coefficient for the $N(z)$ at five pivot redshifts from our Markov Chains (see the Appendix). We find the correlation is weak ($\sim$10%) between adjacent N_i pivots for each SPIRE band.

Two additional $N(z)$ predictions from the literature are also shown in the plot for comparison. The dashed line is a direct estimate of $N(z)$ from PSF-fitted extraction using 24 μm positions as a prior (Béthermin et al. 2012) and the green curve is a model prediction for the SPIRE redshift distribution (Béthermin et al. 2010). Our estimation for $N(z)$ for the 250 μm band agree well with both the direct extraction based on 24 μm identifications and a model prediction, while we find some differences at 350 and 500 μm. However, given the large uncertainties in our binned $N(z)$ estimate these differences are statistically insignificant.

In addition to $N(z)$ and bias factors of SPIRE-selected galaxies, we also measure the bias factors of the optical and IR-selected galaxy samples that we have used for cross-correlations. In Figure 6, we show the two-dimensional error plots, and in Table 2 we list the best-fit bias values and their uncertainties. These results are obtained by combining the likelihoods from the MCMC chains of all three SPIRE bands. These values are consistent with values quoted in the literature for the bias of these samples. For example, the DOGs have an estimated bias factor of 3.1 ± 0.5 (Browdin et al. 2008), which can be compared to our estimate of $2.6^{+1.1}_{-1.9}$. While fully consistent with the Browdin et al. (2008) estimate, our central value is lower than their value, as we account for the full redshift distribution of these galaxies, while their analysis assumed a redshift of 2 for the whole DOG sample in the Boötes field.

In Figure 7, we show the 68% confidence contour maps of the bias factors of SPIRE sources at the three wavelengths (the values and uncertainties are listed in Table 1). We generally find that the SPIRE galaxy bias factors are consistent with $b(z) \sim 1 + z$ (i.e., $c \approx 1$). To understand further the evolution of the sub-mm galaxy bias factor, we plot the redshift dependence in Figure 8, where we compare with the bias factor of dark matter halos at several halo masses, from dwarf galaxy mass to galaxy cluster scales. The bias factors we find at all three wavelengths indicate a halo mass in the range of few times 10^{10} to few times 10^{13} $M_\odot$. The SPIRE clustering analysis in Cooray et al. (2010) found a halo mass for sub-mm galaxies that is about

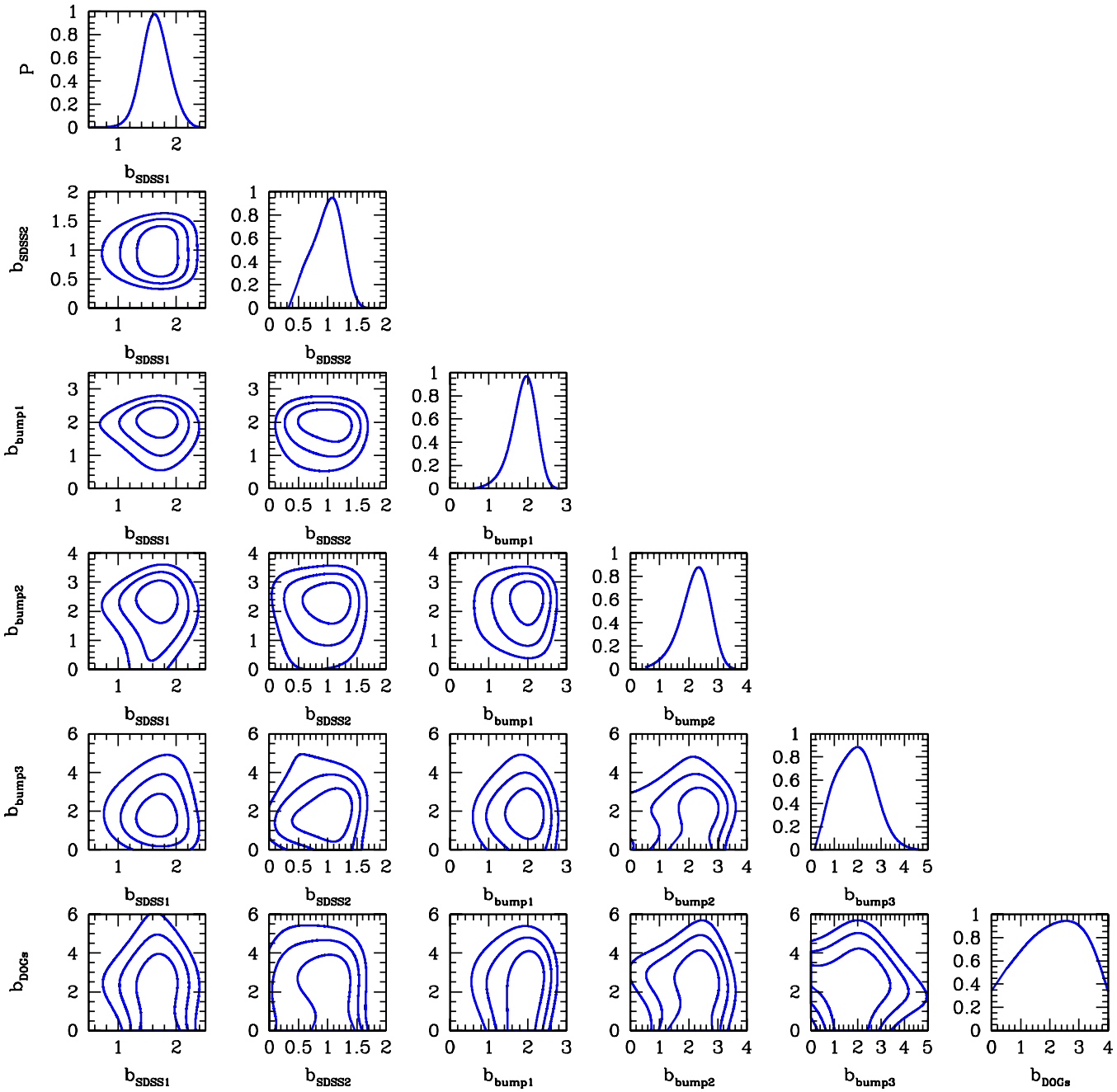

Figure 6. One- and two-dimensional probability distribution functions for bias parameters for all of the Boötes samples used throughout this paper. These bias parameters are estimated by combining the likelihoods from the MCMC chains of all three SPIRE bands. The 68.3%, 95.5%, and 99.7% uncertainties from the fits are shown in the two-dimensional error plots.

(A color version of this figure is available in the online journal.)

$3 \times 10^{12}\ M_{\odot}$, under the assumption of a redshift distribution for the sub-mm galaxy population with a peak at $z \sim 2.3$, similar to the DOG redshift distribution in Figure 2. We now find a slightly lower bias factor, and this is primarily due to the fact that the underlying redshift distribution of the SPIRE galaxies, especially at 250 μm, contains more sources at lower redshifts ($z \lesssim 1$). While the result here is for bright sub-mm sources that are individually detected, the model interpretation of the SPIRE anisotropy power spectrum by Amblard et al. (2011) found a minimum halo mass of $3 \times 10^{11}\ M_{\odot}$.

In Figure 8 we also compare the SPIRE sub-mm galaxy bias factors to samples of galaxies and quasars from the literature (Shen et al. 2007; Ross et al. 2009; Hickox et al. 2012). Our results are generally consistent with the possibility that submillimeter galaxies (SMGs) and quasars trace similar evolutionary paths and that the hosts correspond to dark matter halos that contain a $\sim$ few $L_{\star}$ ellipticals at $z \sim 0$. The exact mechanism on how the starburst galaxies seen in SPIRE feed the black holes that result in the quasars, and the subsequent feedback that suppresses star formation, remains uncertain.

In Figure 8, we also plot two models for the evolution of the bias factor of merging galaxies from Hopkins et al. (2008). While these models have similar behavior at $z < 3$, differences exist at higher redshift. A clustering study of SPIRE-

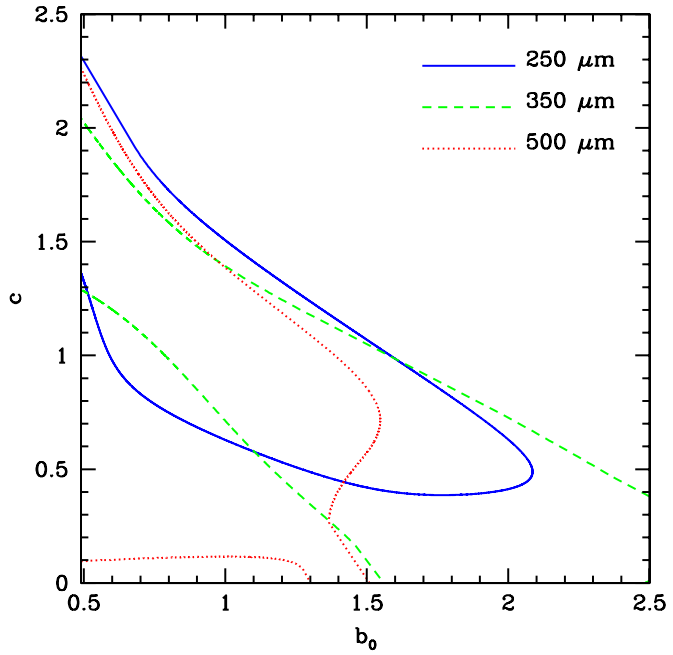

Figure 7. 68% contour maps of the bias parameters b_0 and c, determined from the MCMC analysis, at 250, 350, and 500 μm with $S > 20$ mJy in the Boötes field.

(A color version of this figure is available in the online journal.)

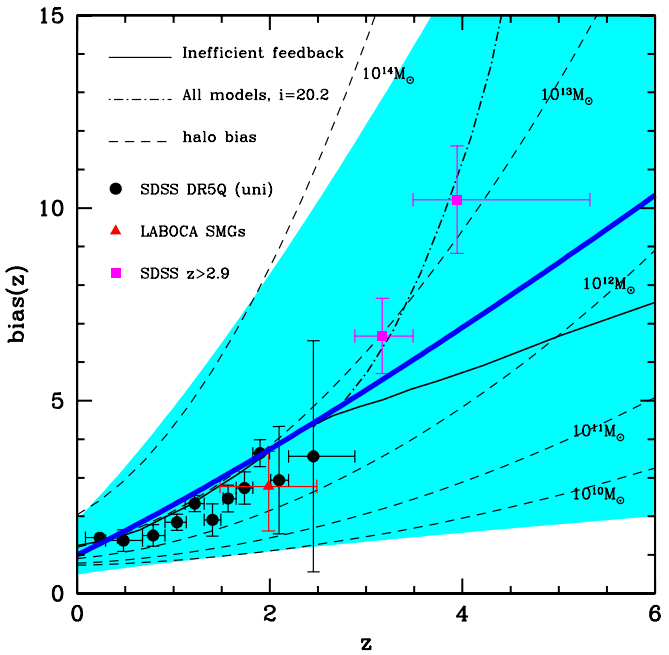

Figure 8. Clustering bias of $S_{350} > 20$ mJy SPIRE sources as a function of redshift. The shaded region shows the 68% confidence region allowed, with the blue solid line showing the best-fit $b(z)$ relation. For reference we plot the bias factor of dark matter halos as a function of halo mass. The range allowed by the data over $0 < z < 4$ is occupied by halos with mass $10 < \log M/M_{\odot} < 14$. We also show samples of galaxies and quasars from the literature (Shen et al. 2007; Ross et al. 2009; Hickox et al. 2012), and two models for the evolution of the bias factor of merging galaxies from Hopkins et al. (2008) involving all three models at $i = 20.2$ (dash-dotted lines) and inefficient (black solid) feedback.

(A color version of this figure is available in the online journal.)

selected sub-mm galaxies at $z > 4$ on its own, or as a cross-correlation with high-redshift quasars, could potentially be used to understand the intricate role of starbursts and quasars and to separate the subsequent feedback processes.

7. CONCLUSIONS

The wide-area sub-mm surveys with the SPIRE instrument aboard the *Herschel Space Observatory* have now led to catalogs of the order of one-hundred-thousand dusty, star-forming galaxies at 250, 350, and 500 μm. While some properties of this sub-mm source population are now understood, the redshift distribution of these galaxies, $N(z)$, is not yet well-determined observationally. We make a statistical estimate of $N(z)$ using a clustering analysis involving the cross-correlation of sub-mm galaxies detected at each of 250, 350, and 500 μm from the HerMES centered on the Boötes field, against samples of galaxies detected at optical and near-IR wavelengths from the SDSS, the NDWFS, and the SDWFS.

We create optical and near-IR galaxy samples based on their photometric or spectroscopic redshift distributions and test the accuracy of these redshift distributions with similar galaxy samples defined via catalogs of the COSMOS. We fit the clustering auto and cross-correlations of SPIRE and optical/IR galaxy samples at angular scales of $0.^{\circ}1$–1°, where clustering of each of the galaxy samples is expected to be linear, with the amplitude determined by a bias factor together with the redshift distribution of the sources. We make use of an MCMC method to sample $N(z)$ at five nodes in the range $0 < z < 4$, as well as the bias factors. The SPIRE-selected sub-mm galaxy bias factor is found to vary with redshift according to $b(z) = 1.0^{+1.0}_{-0.5}(1+z)^{1.2^{+0.3}_{-0.7}}$. We find clear evidence of evolving redshift distributions as the wavelength increases from 250 μm to 500 μm, with the 250 μm band containing the largest number of low-redshift sources. We also compare the measured redshift distribution to model predictions in the literature, and find an excess of sources in the highest redshift bin when compared to the model prediction from Béthermin et al. (2010), although in general our results agree with both predictions from the literature. With subsequent observations in more fields, this analysis could potentially be carried out again—incorporating more data in this analysis would reduce the size of the errors and more fully constrain the $N(z)$ of these sub-mm galaxies.

SPIRE has been developed by a consortium of institutes led by Cardiff University (UK) and including: the University of Lethbridge (Canada); NAOC (China); CEA, LAM (France); IFSI, the University of Padua (Italy); IAC (Spain); Stockholm Observatory (Sweden); Imperial College London, RAL, UCL-MSSL, UKATC, the University of Sussex (UK); and Caltech, JPL, NHSC, the University of Colorado (USA). This development has been supported by national funding agencies: CSA (Canada); NAOC (China); CEA, CNES, CNRS (France); ASI (Italy); MCINN (Spain); SNSB (Sweden); STFC, UKSA (UK); and NASA (USA).

The data presented in this paper will be released through the HeDaM Database in Marseille. This work made use of images and/or data products provided by the NOAO Deep Wide-Field Survey, which is supported by the National Optical Astronomy Observatory (NOAO). NOAO is operated by AURA, Inc., under a cooperative agreement with the National Science Foundation.

Funding for the SDSS and SDSS-II has been provided by the Alfred P. Sloan Foundation, the Participating Institutions, the National Science Foundation, the U.S. Department of Energy, the National Aeronautics and Space Administration, the

Table 3
The Correlation Coefficient of the $N(z_i)$ at Five Pivot Redshifts for Three SPIRE Bands

	250 μm					350 μm					500 μm				
	N_1	N_2	N_3	N_4	N_5	N_1	N_2	N_3	N_4	N_5	N_1	N_2	N_3	N_4	N_5
N_1	1.00					1.00					1.00				
N_2	−0.03	1.00				0.00	1.00				0.05	1.00			
N_3	−0.02	−0.18	1.00			0.00	−0.03	1.00			0.09	0.00	1.00		
N_4	0.08	−0.10	−0.05	1.00		−0.11	−0.09	−0.05	1.00		0.12	0.04	−0.06	1.00	
N_5	−0.01	−0.01	−0.06	−0.10	1.00	0.05	0.10	0.02	−0.13	1.00	0.06	0.07	−0.16	−0.11	1.00

Japanese Monbukagakusho, the Max Planck Society, and the Higher Education Funding Council for England. The SDSS Web site is http://www.sdss.org/. The SDSS is managed by the Astrophysical Research Consortium for the Participating Institutions. The Participating Institutions are the American Museum of Natural History, the Astrophysical Institute Potsdam, the University of Basel, the University of Cambridge, Case Western Reserve University, the University of Chicago, Drexel University, Fermilab, the Institute for Advanced Study, the Japan Participation Group, Johns Hopkins University, the Joint Institute for Nuclear Astrophysics, the Kavli Institute for Particle Astrophysics and Cosmology, the Korean Scientist Group, the Chinese Academy of Sciences (LAMOST), Los Alamos National Laboratory, the Max-Planck-Institute for Astronomy (MPIA), the Max-Planck-Institute for Astrophysics (MPA), New Mexico State University, The Ohio State University, the University of Pittsburgh, the University of Portsmouth, Princeton University, the United States Naval Observatory, and the University of Washington.

K.M.W., Y.G., A.C., J.S., and J.L.W. are supported by NASA funds for U.S. participants in *Herschel* through an award from JPL. A.C. and Y.G. also acknowledge support from NSF CAREER AST-0645427 (to A.C.) and K.M.W. acknowledges support from a NSF REU supplement. S.O., A.S., and L.W. acknowledge support from the Science and Technology Facilities Council (grant No. ST/F002858/1) and (grant No. ST/I000976/1). A.F., L.M., and M.V. were supported by the Italian Space Agency (ASI Herschel Science Contract I/005/07/0).

APPENDIX

THE CORRELATION COEFFICIENT OF THE $N(Z)$

In Table 3, we show the correlation coefficient of the $N(z)$ at five pivot redshifts (N_i) for three SPIRE bands, which is derived from our Marcov Chains. The definition is given by

$$r = \frac{\mathrm{cov}(N_i, N_j)}{\sigma_{N_i}\sigma_{N_j}}. \quad \text{(A1)}$$

Here $\mathrm{cov}(N_i, N_j)$, σ_{N_i}, and σ_{N_j} are the covariance matrix and standard deviations for N_i and N_j, respectively.

REFERENCES

Abazajian, K. N., Adelman-McCarthy, J. K., Ageros, M. A., et al. 2009, ApJS, 182, 543
Amblard, A., Cooray, A., Serra, P., et al. 2010, A&A, 518, 9L
Amblard, A., Cooray, A., Serra, P., et al. 2011, Nature, 470, 510
Ashby, M. L. N., Stern, D., Brodwin, M., et al. 2009, ApJ, 701, 428
Béthermin, M., Dole, H., Lagache, G., Le Borgne, D., & Penin, A. 2010, Proceedings of Cosmic Radiation Fields: Sources in the Early Universe (CRF 2010) November 9–12, 2010, ed. M. Raue, T. Kneiske, D. Horns, D. Elsaesser, & P. Hauschildt (Desy: Germany), http://pos.sissa.it/cgi-bin/reader/conf.cgi?confid=121, 3
Béthermin, M., Le Floch, E., Ilbert, O., et al. 2012, arXiv:1203.1925
Bessell, M. S., & Brett, J. M. 1988, PASP, 100, 1134
Blake, C., Pope, A., Scott, D., & Mobasher, B. 2006, MNRAS, 368, 732
Browdin, M., Dey, A., Brown, M. J. I., et al. 2008, ApJ, 687, L65
Capak, P., Aussel, H., Ajiki, M., et al. 2007, ApJS, 172, 99
Csabai, I., Budavri, T., Connolly, A. J., et al. 2003, AJ, 125, 580
Cooray, A., Amblard, A., Wang, L., et al. 2010, A&A, 518, L22
Cooray, A., Hu, W., Miralda-Escude, G., et al. 2000, ApJ, 535, L9
Dey, A. 2009, in ASP Conf. Ser. 408, The Starburst–AGN Connection, ed. W. Wang, Z. Yang, Z. Luo, & Zhu Chen (San Francisco, CA: ASP), 411
Dey, A., Soifer, B. T., Desai, V., et al. 2008, ApJ, 677, 943
Dpran, M., & Mueller, C. M. 2004, J. Cosmol. Astropart. Phys., JCAP09(2004)003
Eisenhardt, P. R., Stern, D., Brodwin, M., et al. 2004, ApJ, 154, 48
Gelman, A., & Rubin, D. 1992, Stat. Sci., 7, 457
Griffin, M. J., Abergel, A., Abreu, A., et al. 2010, A&A, 518, L3
Harris, A. I., Baker, A. J., Frayer, D. T., et al. 2012, arXiv:1204.4706
Hastings, W. K. 1970, Biometrika, 57, 97
Hickox, R. C., Wardlow, J. L., Smail, I., et al. 2012, MNRAS, 421, 284
Hopkins, P. F., Hernquist, L., Cox, T., & Keres, D. 2008, ApJS, 175, 356
Huang, J., Cowie, L. L., Gardner, J. P., et al. 1997, ApJ, 476, 12
Ilbert, O., Capak, P., Salvato, M., et al. 2009, ApJ, 690, 1236
Jannuzi, B. T., & Dey, A. 1999, in ASP Conf. Ser. 191, Photometric Redshifts and the Detection of High Redshift Galaxies, ed. R. Weymann, L. Storrie-Lombardi, M. Sawicki, & R. Brunner (San Francisco, CA: ASP), 111
John, T. L. 1988, A&A, 193, 189
Johnson, H. L. 1966, ARA&A, 4, 193
Komatsu, E., Smith, K. M., Dunkley, J., et al. 2011, ApJS, 192, 18
Landy, S. D., & Szalay, A. S. 1993, ApJ, 412, 64
Lapi, A., Gonzalez-Nuevo, J., Fan, L., et al. 2011, ApJ, 742, 24
Lupu, R. E., Scott, K. S., Aguirre, J. E., et al. 2010, arXiv:1009.5983
Marsden, G., Ade, P. A. R., Bock, J. J., et al. 2009, ApJ, 707, 1729
Newman, J. A. 2008, ApJ, 684, 88
Neyrinck, M. C., Szapudi, I., & Rimes, C. D. 2006, MNRAS, 370, L66
Oliver, S. J., et al. 2012, MNRAS, submitted
Peebles, P. J. E. 1980, The Large-Scale Structure of the Universe (Princeton, NJ: Princeton Univ. Press)
Pilbratt, G., Riedinger, J. R., Passvogel, T., et al. 2010, A&A, 518, L1
Pope, A., & Chary, R.-R. 2010, ApJ, 715, L171
Riechers, D. A., Cooray, A., Omont, A., et al. 2011, ApJ, 733, L12
Ross, N. P., Shen, Y., Strauss, M. A., et al. 2009, ApJ, 697, 1634
Sawicki, M. 2002, AJ, 124, 3050
Schneider, M., Knox, L., Zhan, H., & Connolly, A. 2006, ApJ, 651, 14
Scott, K. S., Lupu, R. E., Aguirre, J. E., et al. 2011, ApJ, 733, 29
Scoville, N., Aussel, H., Brusa, M., et al. 2006, arXiv:astro-ph/0612305
Shen, Y., Strauss, M. A., Oguri, M., et al. 2007, AJ, 133, 2222
Simpson, C., & Eisenhardt, P. 1999, PASP, 111, 691
Smith, A. J., Wang, L., Oliver, S. J., et al. 2012, MNRAS, 419, 377
Waddington, I., Oliver, S. J., Babbedge, T. S. R., et al. 2007, MNRAS, 381, 1437
Wang, L., Cooray, A., Farrah, D., et al. 2011, MNRAS, 414, 596
Wright, E. L., Eisenhardt, P., & Fazio, G. 1994, BAAS, 26, 893
Zhang, P., Pen, U.-L., & Bernstein, G. 2010, MNRAS, 405, 359